Reducing the efficiency-stability-cost gap of organic photovoltaics with highly efficient and stable small molecule acceptor ternary solar cells

Derya Baran,[*§] Raja Shahid Ashraf,[*§] David A. Hanifi, Maged Abdelsamie, Nicola Gasparini, Jason A. Röhr, Sarah Holliday, Andrew Wadsworth, Sarah Lockett, Marios Neophytou, Christopher J. M. Emmott, Jenny Nelson, Christoph J. Brabec, Aram Amassian, Alberto Salleo, Thomas Kirchartz, James R. Durrant and Iain McCulloch

Dr. D. Baran, Dr. R. A. Ashraf, Dr. S. Holliday, A. Wadsworth, S. Lockett, Prof. J. R. Durrant, Prof. I. McCulloch
Department of Chemistry and Centre for Plastic Electronics, Imperial College London, London, SW7 2AZ, UK

M. Abdelsamie, M. Neophytou, Prof. A. Amassian, Dr. D. Baran, Prof. I. McCulloch
King Abdullah University of Science and Technology (KAUST), SPERC, Thuwal 23955-6900, Saudi Arabia

J. A. Röhr, C. J. M. Emmott, Prof. J. Nelson,
Centre for Plastic Electronics, Department of Physics, Imperial College London, London SW7 2AZ, United Kingdom

J. A. Röhr,
Centre for Plastic Electronics, Department of Chemistry, Imperial College London, London SW7 2AZ, United Kingdom

N. Gasparini, Prof. C. J. Brabec
Institute of Materials for Electronics and Energy Technology (I-MEET), Friedrich-Alexander-University Erlangen-Nuremberg, Erlangen, Germany

D. A. Hanifi, Prof. A. Salleo
Department of Materials Science and Engineering, Stanford University, 476 Lomita Mall, Stanford, California 94305, United States

Dr. D. Baran, Prof. T. Kirchartz,
IEK5-Photovoltaics, Forschungszentrum Jülich, 52425 Jülich, Germany

Prof. T. Kirchartz
Faculty of Engineering and CENIDE, University of Duisburg-Essen, Carl-Benz-Straße 199, 47057 Duisburg, Germany

E-mail: r.ashraf@imperial.ac.uk, d.baran@imperial.ac.uk

Abstract

Technological deployment of organic photovoltaic modules requires improvements in device light-conversion efficiency and stability while keeping material costs low. Here we demonstrate highly efficient and stable solar cells using a ternary approach, wherein two non-fullerene acceptors are combined with both a scalable and affordable donor polymer, poly(3-hexylthiophene) (P3HT), and a high efficiency, low band-gap polymer in a single-layer bulk-heterojunction devices. The addition of a strongly absorbing small molecule acceptor into a P3HT-based non-fullerene blend increases the device efficiency up to 7.7 ± 0.1% without any solvent additives. The improvement is assigned to changes in microstructure that reduces charge recombination and increases the photovoltage, and to improved light harvesting across the visible region. The stability of P3HT-based devices in ambient conditions is also significantly improved relative to polymer:fullerene devices. Combined with a low band gap donor polymer (PBDTTT-EFT, also known as PCE10), the two mixed acceptors also lead to solar cells with 11.0 ± 0.4% efficiency and a high open-circuit voltage of 1.03 ± 0.01V.

Currently, the materials used in organic photovoltaics (OPV) are dominated by fullerene acceptors in combination with low band gap donor polymers which typically require complex and multi-step syntheses.[1-5] However, the commercialization of OPV requires the availability of inexpensive materials in large quantities such as poly(3-hexylthiophene) (P3HT). P3HT is readily scalable via flow or micro-reactor synthesis, even using 'green' solvents, whilst retaining a high degree of control over molecular weight and regio-regularity.[6] The P3HT:60PCBM blend exhibits one of the most robust microstructures within OPV.[7-9] However, it has a limited open-circuit voltage (V_{oc}) and short-circuit current (J_{sc}) in photovoltaic devices.[10] We have recently shown that solar cells using an alternative small molecule non-fullerene acceptor (NFA), IDTBR, when mixed with P3HT, can achieve power conversion efficiencies of up to 6.4%.[11] These results have revived interest in the use of P3HT for high performing devices and non-fullerene acceptors.[12-18] The combination of stability, cost and performance for P3HT:NFA devices, make them a compelling choice for commercialization of OPV compared to devices using fullerenes, for which the high costs and energy involved are prohibitive for large scale production.

Recently, multi-component heterojunctions (ternary or more) have emerged as a promising strategy to overcome the power conversion efficiency (PCE) bottleneck associated with binary bulk-heterojunction (BHJ) solar cells.[3,4,19-23,24] However, simultaneous increase in the V_{oc}, J_{sc} and *FF* is a challenge in the ternary approach because of the trade-off between photocurrent and voltage.[23,25,26] Reports show ternary blends using fullerene acceptors, where the V_{oc} is increased using a second acceptor (A_2) with a higher electron affinity (*EA*) than A_1;[23,27-29] however, very few examples of two-acceptor ternary blend devices could surpass the overall efficiency of their respective binary blends.[24,30,31] Therefore, the majority of studies on ternary solar cells have focused on multi-polymer donor:acceptor blends.[19,23,27-29] However, the mixing of two polymers is more complicated due to both a lack of entropic driving force for mixing, and the potential for strong intermolecular attractions between polymer chains.[32] Therefore, a ternary approach, wherein small molecule acceptors are mixed in a donor:multi-acceptor blend ($D:A_1:A_2$, where D is donor polymer, A_1 is the primary acceptor and A_2 is a second acceptor), has the potential to offer morphological advantages. Small molecule NFAs have already reached

>10% PCEs in binary BHJ devices with low bandgap donor polymers;[33] however, their potential in multi-component junctions has not yet been explored.

Here, we demonstrate highly efficient solar cells by both combining P3HT with two NFAs in a ternary blend, as well as extending this approach to utilise a high efficiency low bandgap polymer PCE10, in place of P3HT. Through optimizing the acceptor phase loading ratio in a D:A_1:A_2 blend, and molecular packing with respect to the binary blend, we demonstrate a concurrent improvement in J_{sc}, V_{oc} and FF resulting in a PCE of 7.7± 0.1% % for P3HT cells. These improvements motivated using the D:A_1:A_2 concept with a high performing PCE10, which yields 11.0 ± 0.4% efficiency in single layer ternary devices. Although these high efficiency devices outperform the P3HT devices, the ease of synthesis of the NFAs and P3HT blend, relative to typical low band gap polymer: $PC_{70}BM$ combinations, has the potential to greatly benefit the effective cost of solar energy production.

Characterization of neat materials and blends

Previously, we have shown that a NFA containing an indacenodithiophene core flanked with benzothiadiazole and rhodanine groups, named IDTBR (A_1), can deliver 6.4% PCE in a solar cell device when combined with P3HT (D), which is the highest P3HT:NFA performance reported.[11] In order to further boost the efficiency of P3HT devices, we include three different NFAs as third components (A_2) in a P3HT:IDTBR blend (see Figure 1). In this instance, A_2 is either i) the fluorene-core analogue of IDTBR (FBR),[12] ii) a new indenofluorene analogue of IDTBR called IDFBR (see Supporting Information),[12,34] or iii) 60PCBM, which is the most investigated acceptor molecule used in combination with P3HT in BHJ solar cells. Unlike 60PCBM, both FBR and IDFBR have linear, donor-acceptor molecular structures similar to IDTBR, including having flanking rhodanine and benzothiadiazole units.[11,12] From the energy level diagram shown in Figure 1b, FBR and IDFBR have a 0.1-0.2 eV lower EA compared to IDTBR as measured by thin film cyclic voltammetry (CV). UV-vis absorption spectra of solutions and thin films determined the spectral range of each material in the visible region (Figure 1c). Relative to 60PCBM, the absorption spectra of FBR and IDFBR show significantly stronger absorption with absorption maxima (λ_{max}) at around 510 nm and 530 nm, respectively. Furthermore, both FBR and IDFBR have complementary absorption spectra to that of IDTBR, which has a λ_{max} at 690 nm and absorption that extends into the near-IR region. The non-fullerene acceptors have extinction coefficients at their absorption maxima that are an order of magnitude greater than 60PCBM (4.9 × 10-6 to 2.3 × 10-5 M) in the visible (see Figure 1d) which should assist increased photon harvesting in solar cells (Table S1). The UV-vis absorption spectra of binary and ternary blend films show interesting phenomena upon annealing at 130°C for 10 min. The absorption spectrum of the P3HT:IDTBR film exhibits a significant red-shift of about 40 nm in the low energy peak upon annealing, which is ascribed to a high degree of aggregation of IDTBR in the film. However, there is no observed shift upon annealing of any of the ternary P3HT:IDTBR:A_2 blends, indicating that the aggregation of IDTBR is suppressed in the ternary blend (Figure S1b).

Morphology picture of the ternary blends

In order to elucidate the role of the A_2 in the ternary blends we carried out differential scanning calorimetry (DSC) and *in-situ* grazing incidence wide angle X-ray scattering (GIWAXS) measurements during spin coating of P3HT:IDTBR:A_2 ternary films from chlorobenzene solution (Higher resolution diffraction patterns were collected *ex situ*, as discussed below). The relative degree of crystallinity of the donor for each ternary blend was calculated by fitting the GIWAXS spectra (Figure S2a).[35-37] *In situ* GIWAXS measurements suggest that, in all ternary blends, P3HT crystallization appears at the very end of solvent evaporation, as characterized by a sharp increase in scattering intensity associated with P3HT lamellar stacking and a sharp decrease in solvent scattering intensity (Figures S2a and S2b).[35,38] The unperturbed P3HT crystallization can be understood by the fact that P3HT reaches supersaturation in solution and starts to crystallize earlier than all of the other components, which is further supported by *in-situ* UV-vis absorption measurements performed during spin coating (Figure S3).[38] GIWAXS measurements performed on as-cast and thermally annealed (130°C) films are also summarized in Figures S2c and S2d, respectively. The crystalline correlation length (CCL) and the relative crystallinity of the P3HT phase for each of the ternary blends have been calculated in Table S2.[39] The as-cast P3HT:IDTBR:60PCBM blend exhibits the lowest P3HT crystallinity and CCL (corresponding to the smallest crystallite size). P3HT:IDTBR:IDFBR exhibits the highest relative crystallinity amongst ternary films, indicating more pronounced polymer:small molecule phase separation for both the as-cast and annealed films.

DSC profiles of P3HT, IDTBR and IDFBR in the neat, binary and the best performing P3HT:IDTBR:IDFBR ternary blend are presented in Figure 2a. The heat flow profiles reveal that both the IDFBR and IDTBR binary blends with P3HT exhibits broad endothermic transitions at temperatures above 200 °C, attributed to a P3HT crystalline phase melt. In comparison to the pristine P3HT, the melting transition of P3HT is broadened and suppressed in all blends, most significantly in the P3HT:IDFBR blend (factor of 5). In the P3HT:IDTBR blend, the P3HT melting endotherm is prominent, although its peak has still been slightly depressed and broadened, and there is a minimal reduction in melting enthalpy. In the ternary blend film, the P3HT crystalline phase still persists, with a broad melt endotherm. The comparison of the binaries indicates that both of the small molecule species can diffuse into the P3HT phase, with IDFBR doing so to a greater extent, leading to more extensive disorder in the polymer, in agreement with *in situ* GIWAXS observations of P3HT crystallization in such blends (Figure S2). The IDTBR crystalline transition in the ternary blend exhibits a melting point depression and lower enthalpy in comparison to the IDTBR binary film, indicating that the IDFBR has been able to also diffuse into the IDTBR phase. No evidence of any IDFBR thermal transitions is present in the ternary. The cooling scan (Figure S4a) shows a strongly super-cooled crystallisation of P3HT, but no small-molecule crystallisation. The ternary film, therefore, can be described as having three partially miscible components, comprising a crystalline P3HT phase, which also hosts a molecular dispersion of IDFBR molecules, as well as an IDTBR-rich crystalline phase that also contains IDFBR. High resolution 2D GIWAXS patterns of P3HT:IDTBR:IDFBR ternary blend were studied to understand the role of IDFBR in the optimized ternary blend (Figure S4b). The change in the intensity of the (300) peak of IDTBR (Q_z ≈0.61 Å $Å^{-1}$) is plotted in Figure 2b as a function of A_1:A_2 phase composition. The annealed P3HT:IDTBR (1:1) binary blend shows prominent crystallinity from both the polymer (reported above) and the acceptor (Figure S4b). The fact that the crystalline structure of P3HT is unperturbed by the presence of IDTBR is in agreement with the small shift of the P3HT melting point observed by DSC. The degree of P3HT crystallinity remains relatively constant upon addition of increasing amounts of IDFBR, while the fraction of IDTBR crystallites steadily decreases as IDTBR is replaced by IDFBR in the blend (Figure S4c). The optimized 1:0.7:0.3 P3HT:IDTBR:IDFBR ternary blend displays remnant crystallinity of the small molecule phase (illustrated schematically in Figure 2c). Above 30% IDFBR addition, the intensity of the IDTBR crystalline peak drops sharply, essentially reducing to noise for all IDFBR compositions up to 70% (Figure S4d and 4e). Hence, it appears that IDFBR dissolves in the P3HT and as its weight fraction is increased, it vitrifies the remaining IDTBR. This makes the acceptor phase a disordered solid solution of the two molecules, while the crystalline order of the polymer appears to be mostly unperturbed.

Photovoltaic device characterization

The photovoltaic parameters for D:A_1 and D:A_1:A_2 devices are summarized in Table 1. Representative current density–voltage (*J*–*V*) characteristics of binary P3HT:IDTBR and P3HT:IDFBR devices and ternary P3HT:IDTBR:IDFBR (1:0.7:0.3) and PCE10:IDTBR:IDFBR (1:0.5:0.5) devices under 1 sun illumination are shown in Figure 3a. The P3HT:IDTBR device exhibits a J_{sc} and *FF* of 13.9 mA cm^{-2} and 0.60, respectively, and a V_{oc} of 0.73 V which is relatively high for a P3HT based solar cell (0.58 V for P3HT:60PCBM), [12] resulting in a PCE of 6.3% (Table S3). The P3HT:IDFBR devices are optimized for an equal 1:1 D:A ratio in CB, which gives remarkably high V_{oc} and *FF* values up to 0.88 V and 0.64, respectively, but a lower J_{sc}, with an overall efficiency of 4.5% (Table S4). In comparison to binary blends, the addition of IDFBR as A_2 in the P3HT ternary blend shows a significant improvement in the overall PCE to 7.7± 0.1% % (Figure 3a). The best P3HT:IDTBR:IDFBR devices are achieved with a ratio of 1:0.7:0.3 (D:A_1:A_2), giving a J_{sc} of 14.4 mA cm^{-2}, *FF* of 0.64 and a V_{oc} of 0.82 V, which lies between those of the two binary devices. Further addition (up to 70%) of IDFBR resulted in V_{oc} values of 0.82 V, but a decrease in J_{sc}, which is mainly attributed to the reduced absorption at long wavelengths from IDTBR in the ternary blend (Figure S5). It is also noteworthy that P3HT:IDTBR:IDFBR devices can retain the high *FF* values of the binaries (0.64) with slightly lower V_{oc} and J_{sc} (0.78 V and 11.3 mA cm^{-2}) with an overall efficiency of

5.7% at thicknesses ~200 nm (Figure S6a). Additionally, larger area P3HT:IDTBR:IDFBR devices (~1 cm^2) have also been demonstrated successfully with efficiencies as high as 6.5% with slightly lower *FF* (Figure S6b) (Table S5). The substitution of IDFBR with either 60PCBM or FBR as A_2 gave significantly inferior results compared to the P3HT:IDTBR:IDFBR device performance, which is further detailed in the supplementary information. PBDTTT-EFT (PCE10) has recently attracted attention in polymer:NFA solar cells due to its high efficiency with fullerene derivatives and its absorption in the low energy region in the spectrum.[32] In order to validate that using two NFAs can yield state of the art photovoltaic performances, we used a low band gap polymer PCE10 with the same NFA acceptors in ternary solar cells. The un-optimized preliminary results showed that a PCE of 11.0 ± 0.4% is achievable with a V_{oc} of 1.03 V, a high J_{sc} of 17.3 mA/cm^2 and a decent FF of 0.61 using 1:0.5:0.5 PCE10:IDTBR:IDFBR ratio without the need for any processing additive or heat treatment (Table 1). These results showed that the potential of high performing polymers such as PCE10 can be boosted with A_1:A_2 approach using NFAs.

External quantum efficiency (EQE) spectra of binary P3HT:IDTBR and P3HT:IDFBR devices and the best ternary P3HT:IDTBR:IDFBR (1:0.7:0.3) and PCE10:IDTBR:IDFBR (1:0.5:0.5) devices are shown in Figure 3b. Relative to the maximum P3HT:IDTBR EQE of 55% (λ_{max} at 500 nm), the maximum EQE of the P3HT:IDTBR:IDFBR blend shows a substantial increase up to 70% in the 400-700 nm region, which explains the integrated photocurrent enhancement in the EQE for P3HT:IDTBR:IDFBR device. The high photocurrent of the PCE10:IDTBR:IDFBR ternary cells is confirmed with EQE measurements where the photo-conversion >70% is observed between 500-700 nm reaching a maximum of 85% around 700 nm. The integrated photocurrent from the EQE spectrum of PCE10 ternary solar cells is consistent with the device J_{sc} values confirming the very high photocurrent generation in the ternary devices. In all cases, the increased maximum EQE can be explained by improved light harvesting in the region where both polymer and A_2 absorb. However, the reduced EQE values beyond 500 nm, due to the low absorption strength of 60PCBM and, to some extent, of FBR, limits the J_{sc} from these ternary blends compared to the P3HT:IDTBR device (Figure S6c).

Charge transport and recombination

In order to explain the simultaneous increase in V_{oc}, J_{sc} and *FF* in the P3HT:IDTBR:IDFBTR device compared to P3HT:IDTBR, we performed charge extraction (CE), transient photo-voltage (TPV) (at V_{oc}) and space-charge-limited current (SCLC) measurements.[22,40] These measurements, in combination with sensitive EQE (where a lock-in is used to increase the signal/noise ratio) and electroluminescence (EL),[41] were utilized to explain the charge transport, recombination behaviour and the origin of the increased V_{oc} in the P3HT:IDTBR:IDFBR blend from different perspectives. Charge extraction data were used to determine the average excess charge carrier density (Δn) of P3HT:IDTBR and P3HT:IDTBR:IDFBR (1:0.7:0.3) blends as a function of background light intensity, to allow V_{oc} to be plotted against Δn as shown in Figure 4a; these data allow the effective electronic band gap of different blends to be compared. The approximately 90 meV shift in the V_{oc} for the P3HT:IDTBR:IDFBR device relative to P3HT:IDTBR is indicative of a larger effective band gap for ternary blends. This can be attributed to inhibition of IDTBR aggregation in the ternary blend; where molecular aggregation typically reduces electronic and optical bandgaps, with the latter being apparent from the UV-vis absorption data discussed above. This increased electronic band gap for the ternary blend is likely to be the primary reason for the increased voltage output of ternary device (Table 1).[40]

The trend in V_{oc} for the P3HT:IDTBR:IDFBR blend with IDFBR fraction can further be analysed using the EQE spectra of ternary compositions. The low energy onset of EQE in these systems is dominated by photo-generation in the acceptor and the EQE trend therefore indicates the shift in acceptor optical gap with composition (Figure S7). The broadening optical gap, resulting from inhibition of aggregation in the IDTBR will result partly from an upward shift in acceptor EA (note that the CV data presented in Figure 1 were for a pristine, and therefore crystalline, thin film of IDTBR) and should indicate the trend in V_{oc}.[41-43] Figure 4b directly compares the photon energies (at EQE = 10^{-2} %) of P3HT:IDTBR:IDFBR ternary devices and the V_{oc} as a function of IDFBR content. A clear trend is visible with a ~80 ± 10 meV increase in optical gap for the 1:0.7:0.3 blend relative to the binary blend, which is in agreement with the 90 meV difference in V_{oc} between P3HT:IDTBR:IDFBR (1:0.7:0.3) and P3HT:IDTBR devices. EL measurements, which usually probe the lowest emissive states in a blend, confirm an energetic blue shift for P3HT:IDTBR:IDFBR devices compared to P3HT:IDTBR devices (Figure S7b). Note that the shift in absorption edge may not entirely account for the shift in V_{oc}, since part of the optical gap enlargement may be due to a decrease of the acceptor IP, and not only a raise in the EA, as IDTBR crystallization is suppressed. Therefore we investigate the effect of IDFBR addition on charge recombination via the charge carrier lifetime.

The carrier lifetime of P3HT:IDTBR:IDFBR (1:0.7:0.3) was measured using TPV to be 17 µs (at 1 sun), which is two to three times longer than that measured for P3HT:IDTBR (6.5 µs) (Figure 4c). As discussed above, IDFBR exhibits a higher-lying EA than IDTBR and is more miscible with P3HT, such that IDFBR is likely to accumulate in the mixed regions around the P3HT. The P3HT:IDFBR interface presents an energetic barrier to charge recombination of electrons in the (amorphous or crystalline) IDTBR with P3HT holes (i.e.: a three component redox cascade). Whilst such a cascade is also likely to exist in the mixed phase of the binary system, the higher lying LUMO of IDFBR compared to amorphous IDTBR will enhance the cascade effect in the ternary. This increased lifetime is likely to contribute a further 30-40 mV increase for the V_{oc} of ternary P3HT:IDTBR:IDFBR device.[44] A second reason for extended charge carrier lifetime in the ternary blend is the increased degree of electron trapping, evident from the SCLC measurements (Figure S8). The presence of traps in the binary is supported by the vitrification of the IDTBR crystallinity into an amorphous solid at 1:0.7:0.3 ratio (Figure S4). In an amorphous material, a small amount of a crystalline phase will act as trap sites.[45] SCLC of electron-only IDTBR (μ_e = 5.35 x 10^{-4} $cm^2V^{-1}s^{-1}$) and IDTBR:IDFBR (0.7:0.3) (μ_e = 5.45 x 10^{-4} $cm^2V^{-1}s^{-1}$) devices,[46] indicate a higher density of electron trap states in the 30% IDFBR blend but otherwise very similar electron transport. (Figure S8).

Operational stability and energy return on investment

In order to be compatible with manufacturing processes, a solar cell device should be comprised of scalable materials as well fabricated by easy processing without solvent additives which has been shown to be detrimental to stability.[47] In addition, the devices need to exhibit ambient-stability during fabrication as well as during operation. We tested the ambient stability of our ternary and binary devices and compared these results with a range of high efficiency low band gap polymer:fullerene solar cells, fabricated (in air) using commercially available polymers. Devices were stored at room temperature, under both dark (Figure 5) and light (1 sun) conditions (Figure S9)). After 1200 h in air and under dark conditions, the ternary P3HT:IDTBR:IDFBR (1:0.7:0.3) device retains 80% of its PCE (6.1%), while P3HT:IDTBR performance retained 70% (4.3%). However, all of the low band gap polymer:fullerene blends were no longer operational after only 800 h in air (Figure S9). In addition, we exposed high efficiency polymer:fullerene, P3HT:NFA and P3HT:IDTBR:IDFBR devices at operating conditions (un-encapsulated, in air, AM1.5 radiation to illumination 100 $mWcm^{-2}$) for an initial 90 h test (Figure 9c). The P3HT:IDTBR:IDFBR device exhibited the best air photo-stability, retaining 85% of its initial performance after 90 h. Meanwhile, the high efficiency PCE10:$PC_{70}BM$ device performance dropped to 20% of its initial value. These results suggest that the addition of IDFBR to P3HT:IDTBR blend not only improves photovoltaic performance but also has a synergistic benefit to both storage lifetime and photo-stability, which demonstrates a significant advantage for practical applications in comparison to low band gap:fullerene solar cells.

It is generally accepted that the main conditions for economically viable electricity generation by thin film photovoltaics are high efficiency, low cost (represented here by ease of synthesis at the lab scale) and extended lifetime. Energy return on investment (EROI)[48] is a measure of the energy yield from the PV device relative to the energy invested in synthesis and manufacture. Drawing on published estimates of the embodied energy in polymer and molecule synthesis and device processing,[49,50] the efficiencies of different device designs and relative stabilities demonstrated here in Figure 5a, we estimate (see supporting information for EROI) that the embodied energy of a polymer encapsulated P3HT:NFA device is at least as low as that of a similarly encapsulated, higher efficiency polymer: $PC_{70}BM$ device, and that the EROI around a factor of 5 higher and is the highest of any material system studied. The advantage in EROI arises in large part from the higher stability of the P3HT:NFA device shown in Figure 5a, This suggests that a P3HT:NFA based technology will be the most cost effective of the technologies considered in production.

In conclusion, we report highly efficient P3HT (7.7± 0.1% %) and PCE10 (PBDTTT-EFT) (11.0± 0.4%) based BHJ ternary solar cells in an inverted architecture fabricated using two non-fullerene acceptors. By optimizing the second acceptor component in a P3HT ternary blend, we have created an optimal phase morphology wherein the vitrification of the crystalline IDTBR phase by IDFBR that leads to preservation of the three phase microstructure that is favourable for photocurrent generation. This optimal phase morphology yields a higher lying electron transport level (benefitting V_{oc}), reduced bimolecular recombination and a preserved collection efficiency, resulting in a simultaneous improvement in V_{oc}, J_{sc} and FF for P3HT:IDTBR:IDFBR devices. The PCE10 preliminary results also show that two NFA ternary approach can further boost the PCE of high efficiency potential polymers. This demonstration revives the use of P3HT in high performance OPV devices closing the gap between the efficiency, lifetime, energy efficiency and cost requirements needed in order to commercialize OPV.

Additional information

Supplementary information is available in the online version of the paper. Reprints and permissions information is available online at www.nature.com/reprints. Correspondence and requests for materials should be addressed to D. B., R. S. A and I. M.

Competing financial interest

The authors declare no competing financial interests.

Acknowledgements

DB thanks Helmholtz Association for a Helmholtz Postdoc Fellowship.

S.H. thanks BASF for financial support. The authors acknowledge EC FP7 Project SC2 (610115), EC FP7 Project ArtESun (604397), and EPSRC Project EP/G037515/1, EC FP7 Project POLYMED (612538) and Project Synthetic carbon allotropes project SFB 953.

Author Contributions

D.B and R.S.A. prepared the manuscript. S. H. and A. W. synthesized the non-fullerene acceptors. R.S.A. fabricated and characterized solar cell devices. D. B. and N. G. carried out CE and TPV measurements. M.A. performed the in situ GIWAXS and UV-vis absorption measurements during spin coating. D.A.H. performed static GIWAXS measurements. J.R. did the SCLC measurements. S.L. performed the DSC measurements. R.A.J and M.N. performed stability measurements. C.J.M.E. helped J. N. with EROI modelling. All authors discussed the results and commented on the manuscript. C.J.B. supervised photo-CELIV, CE. J.D. supervised TPV, A.A. supervised *in situ* GIWAXS and UV-vis measurements, A.S. supervised static GIWAXS, T.K and J.N. supervised SCLC, EL and EQE. I.M. revised the manuscript and supervised and directed the project.

§ D. B and R. S. A contributed equally to this work

Methods

Materials:

All materials are purchased from Sigma Aldrich except 60PCBM from Solenne. PCE10 is supplied from CalOS Organic semiconductors.

Characterization:

^{1}H and ^{13}C NMR spectra were collected on a Bruker AV-400 spectrometer at 298 K and are reported in ppm relative to TMS. UV-Vis absorption spectra were recorded on a UV-1601

Shimadzu UV-Vis spectrometer. Differential Scanning Calorimetry (DSC) experiments were carried out with a Mettler Toledo DSC822 instrument at a heating rate of 5 °C/min under nitrogen. Samples were prepared by drop-casting the materials from $CHCl_3$ solution directly into the DSC pan and allowing the solvent to evaporate under Ar. GIXD was done at beamline 7.3.3 Lawrence Berkeley National Lab (LBNL). The sample was secured inside a helium chamber, with O_2 levels below 1%. The X-ray wavelength was 1.24 Å (10 keV), and the sample was irradiated at a fixed incident angle of 0.125 degrees. The scattering patterns were recorded using a Pilatus 2M detector at a fixed distance of 287.377mm. 2D data reduction were analyzed using Nika 2D software package and peak information was accessed by guassian fitting. Samples for GIWAXS were spin-coated on Si (100) substrates following the same spin-coating and annealing procedures as were used in fabricating solar cells.

In situ grazing incidence wide angle x-ray scattering measurements (GIWAXS):

In situ GIWAXS experiments were performed using a setup described in previous work[35,36] at beam-line D1 at the Cornell High Energy Synchrotron Source, Wilson Lab, NY, USA. The scattering pattern during the spin coating process was recorded using a fast 2D detector (PILATUS 200 k from Dectris) with an exposure time of 0.18 seconds. The wavelength of incident X-ray beam was 1.1555 Å. The sample-to-detector-distance was set to 173.756 mm. The incident angle of the X-ray beam with respect to the sample plane was 0.17°. Calibration of the lengths in the reciprocal space was done by using silver behenate.

In situ UV-Vis absorption measurements during spin-coating:

In situ UV-Vis absorption measurements were performed using a setup described previously.[37] An integration time of 0.2 s per absorption spectrum was used to collect the transmission measurements. The following equation $[A_\lambda = -\log_{10}(T)]$ was used to calculate the UV-vis absorption spectra from the transmission spectra, where A_λ is the absorbance at a certain wavelength (λ) and T is the transmitted radiation.

OPV devices:

The photovoltaic performance of the binary and ternary blend solar cells was measured with a device architecture comprising of: indium tin oxide (ITO)/ zinc oxide (ZnO)/ active layer (85 ± 5 nm) /molybdenum oxide (MoO_3)/Ag, where the active layer consists of either D:A_1 or D:A_1:A_2. Glass substrates were used with pre-patterned indium tin oxide (ITO). These were cleaned by sonication in detergent, deionized water, acetone and isopropanol, followed by oxygen plasma treatment. ZnO layers were deposited by spin-coating a zinc acetate dihydrate precursor solution (60 µl monoethanolamine in 2 ml 2-methoxyethanol) followed by annealing at 150 °C for 10-15 min, giving layers of 30 nm. The active layers were deposited from 20 mg/mL solutions in chlorobenzene by spin-coating at 2000 rpm, followed by annealing at 130 °C for 10 min. Active layer thicknesses were ~90 nm (averaged over 10 devices) for both acceptor blends. MoO_3 (10 nm) and Ag (100 nm) layers were deposited by evaporation through a shadow mask yielding active areas of 0.045 cm^2 in each device. For device optimization, the ratio of A_2 is varied with respect to A_1 such that the donor:acceptor (D:A) mass ratio is fixed at 1:1. All ternary devices were processed using chlorobenzene (CB) without further processing or solvent additives and active layers were pre-annealed in inert atmosphere at 130 °C for 10 min, which is required for P3HT crystallization.[9] Current density-voltage (*J-V*) characteristics were measured in both forward and backward directions (no difference observed) at room temperature, with 20 mA/s scan speed in air, using a Xenon lamp at AM1.5 solar illumination (Oriel Instruments) calibrated to a silicon reference cell with a Keithley 2400 source meter, correcting for spectral mismatch (active area 0.045 cm^2 using a mask). Efficiencies are reported averaging 12 photovoltaic devices. Incident photon conversion efficiency (IPCE) was measured by a 100 W tungsten halogen lamp (Bentham IL1 with Bentham 605 stabilized current power supply) coupled to a monochromator with computer controlled stepper motor. The photon flux of light incident on the samples was calibrated using a UV enhanced silicon photodiode. A 590 nm long pass glass filter was inserted into the beam at illumination wavelengths longer than 580 nm to remove light from second order diffraction. Measurement duration for a given wavelength was sufficient to ensure the current had stabilized.

J-V measurements for storage and operational stability

The same inverted architecture solar cell devices used for J-V and EQE measurements were then taken to the storage and operational stability measurements. For storage stability, the inverted architecture devices were left in ambient cleanroom conditions (~20 °C, <40% humidity) in dark conditions between each measurement. Data is taken with intervals and solar cell devices were exposed to 100 mW/cm^2 illumination for light measurements. For operational stability measurement, devices were transferred to same ambient cleanroom conditions in order to expose them to air and then J-V measurements were performed under constant 100 mW/cm^2 illumination for 90h.

TPV and CE measurements:

A 405 nm laser-diode was used to ensure the solar cells were approximately in V_{oc} condition. Driving the laser intensity with a waveform generator Agilent 33500B and measuring the light intensity with a highly linear photodiode allowed to reproducibly adjust the light intensity with an error below 0.5% over a range of 0.2 to 4 suns. A small perturbation was induced with a second 405 nm laser diode driven by a function generator from Agilent. The intensity of the short (50 ns) laser pulse was adjusted to keep the voltage perturbation below 10 mV, typically at 5 mV. After the pulse, the voltage decays back to its steady state value in a single exponential decay. The characteristic decay time was determined from a linear fit to a logarithmic plot of the voltage transient and returned the small perturbation charge carrier lifetime. In charge extraction measurements a 405 nm laser diode illuminated the solar cell for 200 µs which was sufficient to reach a constant open-circuit voltage with steady state conditions. At the end of the illumination period, an analog switch was triggered that switched the solar cell from open-circuit to short-circuit (50 Ω) conditions within less than 50 ns.

Space charge-limited current (SCLC):

SCLC measurements were performed on electron-only devices of the structure ITO/TiO_2 TiO_2 /P3HT:acceptor/Ca/Al. The current-voltage characteristics were fitted using a using a drift-diffusion solver.

References

1 Zhao, J. *et al.* A Difluorobenzoxadiazole Building Block for Efficient Polymer Solar Cells. *Adv. Mater.* **28**, 1868-1873 (2016).

2 Hwang, Y.-J., Li, H., Courtright, B. A. E., Subramaniyan, S. & Jenekhe, S. A. Nonfullerene Polymer Solar Cells with 8.5% Efficiency Enabled by a New Highly Twisted Electron Acceptor Dimer. *Adv. Mater.* **28**, 124-131201503801 (2016).

3 Zhang, J. *et al.* Conjugated Polymer–Small Molecule Alloy Leads to High Efficient Ternary Organic Solar Cells. *J. Am. Chem. Soc.* **137**, 8176-8183 (2015).

4 Yang, Y. *et al.* High-performance multiple-donor bulk heterojunction solar cells. *Nat. Photon.* **9**, 190-198 (2015).

5 Li, N. & Brabec, C. J. Air-processed polymer tandem solar cells with power conversion efficiency exceeding 10%. *Energ. Environ. Sci.* **8**, 2902-2909 (2015).

6 Bannock, J. H. *et al.* Continuous Synthesis of Device-Grade Semiconducting Polymers in Droplet-Based Microreactors. *Adv. Funct. Mater.* **23**, 2123-2129 (2013).

7 Huang, Y.-C. *et al.* Small- and Wide-Angle X-ray Scattering Characterization of Bulk Heterojunction Polymer Solar Cells with Different Fullerene Derivatives. *J. Phys. Chem. C* **116**, 10238-10244 (2012).

8 Yin, W. & Dadmun, M. A New Model for the Morphology of P3HT/PCBM Organic Photovoltaics from Small-Angle Neutron Scattering: Rivers and Streams. *ACS Nano* **5**, 4756-4768 (2011).

9 Campoy-Quiles, M. *et al.* Morphology evolution via self-organization and lateral and vertical diffusion in polymer:fullerene solar cell blends. *Nat. Mater.* **7**, 158-164, (2008).

10 Dang, M. T., Hirsch, L. & Wantz, G. P3HT:PCBM, Best Seller in Polymer Photovoltaic Research. *Adv. Mater.* **23**, 3597-3602 (2011).
11 Holliday, S *et al.* High Efficiency and Air Stable P3HT Based Polymer Solar Cells with a New Non-Fullerene Acceptor. *Nat. Commun.*,**7**,1-11 (2016).
12 Holliday, S. *et al.* A Rhodanine Flanked Nonfullerene Acceptor for Solution-Processed Organic Photovoltaics. *J. Am. Chem. Soc.* **137**, 898-904 (2015).
13 Sun, D. *et al.* Non-Fullerene-Acceptor-Based Bulk-Heterojunction Organic Solar Cells with Efficiency over 7%. *J. Am. Chem. Soc.* **137**, 11156-11162 (2015).
14 Liu, Y. *et al.* A Tetraphenylethylene Core-Based 3D Structure Small Molecular Acceptor Enabling Efficient Non-Fullerene Organic Solar Cells. *Adv. Mater.* **27**, 1015-1020 (2015).
15 Li, H. *et al.* Beyond Fullerenes: Design of Nonfullerene Acceptors for Efficient Organic Photovoltaics. *J. Am. Chem. Soc.* **136**, 14589-14597 (2014).
16 Meng, D. *et al.* High-Performance Solution-Processed Non-Fullerene Organic Solar Cells Based on Selenophene-Containing Perylene Bisimide Acceptor. *J. Am. Chem. Soc.* **138**, 375-380 (2016).
17 Lin, H. *et al.* High-Performance Non-Fullerene Polymer Solar Cells Based on a Pair of Donor–Acceptor Materials with Complementary Absorption Properties. *Adv. Mater.* **27**, 7299-7304 (2015).
18 Li, S. *et al.* A spirobifluorene and diketopyrrolopyrrole moieties based non-fullerene acceptor for efficient and thermally stable polymer solar cells with high open-circuit voltage. *Energ. Environ. Sci.* **9**, 604-610 (2016).
19 Khlyabich, P. P., Burkhart, B. & Thompson, B. C. Efficient Ternary Blend Bulk Heterojunction Solar Cells with Tunable Open-Circuit Voltage. *J. Am. Chem. Soc.* **133**, 14534-14537 (2011).
20 Lu, L., Chen, W., Xu, T. & Yu, L. High-performance ternary blend polymer solar cells involving both energy transfer and hole relay processes. *Nat. Commun.* **6**, (2015).
21 Ameri, T. *et al.* Morphology analysis of near IR sensitized polymer/fullerene organic solar cells by implementing low bandgap heteroanalogue C-/Si-PCPDTBT. *J. Mater. Chem. A* **2**, 19461-19472 (2014).
22 Gasparini, N. *et al.* An Alternative Strategy to Adjust the Recombination Mechanism of Organic Photovoltaics by Implementing Ternary Compounds. *Adv. Energ. Mater.***5**, 1501527 (2015).
23 Lu, L., Kelly, M. A., You, W. & Yu, L. Status and prospects for ternary organic photovoltaics. *Nat. Photon.* **9**, 491-500 (2015).
24 Zhang, Y. *et al.* Synergistic Effect of Polymer and Small Molecules for High-Performance Ternary Organic Solar Cells. *Adv. Mater.* **27**, 1071-1076 (2015).
25 Khlyabich, P. P., Rudenko, A. E., Thompson, B. C. & Loo, Y.-L. Structural Origins for Tunable Open-Circuit Voltage in Ternary-Blend Organic Solar Cells. *Adv. Funct. Mater.* **25**, 5557-5563 (2015).
26 Ke, L. *et al.* A Series of Pyrene-Substituted Silicon Phthalocyanines as Near-IR Sensitizers in Organic Ternary Solar Cells. *Adv. Energ. Mater.*,1502355 (2016).
27 Ko, S.-J. *et al.* Improved Performance in Polymer Solar Cells Using Mixed PC61BM/PC71BM Acceptors. *Adv. Energ. Mater.* **5**, 1401687, (2015).
28 Cheng, P., Li, Y. & Zhan, X. Efficient ternary blend polymer solar cells with indene-C60 bisadduct as an electron-cascade acceptor. *Energ. Environ. Sci.* **7**, 2005-2011, (2014).
29 Kang, H. *et al.* Effect of Fullerene Tris-adducts on the Photovoltaic Performance of P3HT:Fullerene Ternary Blends. *ACS Appl. Mater. Interfaces* **5**, 4401-4408 (2013).

30 An, Q. *et al.* Simultaneous Improvement in Short Circuit Current, Open Circuit Voltage, and Fill Factor of Polymer Solar Cells through Ternary Strategy. *ACS Appl. Mater.Interfaces* **7**, 3691-3698 (2015).
31 Huang, T.-Y. *et al.* Efficient ternary bulk heterojunction solar cells based on small molecules only. *J.Mater. Chem. A* **3**, 10512-10518 (2015).
32 Nielsen, C. B., Holliday, S., Chen, H.-Y., Cryer, S. J. & McCulloch, I. Non-Fullerene Electron Acceptors for Use in Organic Solar Cells. *Acc.Chem. Res.* **48**, 2803-2812 (2015).
33 Zhao, W. *et al.* Fullerene-Free Polymer Solar Cells with over 11% Efficiency and Excellent Thermal Stability. Adv. Mater. **28**, 4734-4739 (2016).
34 Setayesh, S., Marsitzky, D. & Müllen, K. Bridging the Gap between Polyfluorene and Ladder-Poly-p-phenylene: Synthesis and Characterization of Poly-2,8-indenofluorene. *Macromolecules* **33**, 2016-2020 (2000).
35 Chou, K. W. *et al.* Spin-Cast Bulk Heterojunction Solar Cells: A Dynamical Investigation. *Adv. Mater.* **25**, 1923-1929 (2013).
36 Perez, L. A. *et al.* Solvent Additive Effects on Small Molecule Crystallization in Bulk Heterojunction Solar Cells Probed During Spin Casting. *Adv. Mater.* **25**, 6380-6384 (2013).
37 Abdelsamie, M. *et al.* Toward Additive-Free Small-Molecule Organic Solar Cells: Roles of the Donor Crystallization Pathway and Dynamics. *Adv. Mater.* **27**, 7285-7292 (2015).
38 Rivnay, J., Mannsfeld, S. C. B., Miller, C. E., Salleo, A. & Toney, M. F. Quantitative Determination of Organic Semiconductor Microstructure from the Molecular to Device Scale. *Chem. Rev.* **112**, 5488-5519 (2012).
39 Richter, L. J. *et al.* In Situ Morphology Studies of the Mechanism for Solution Additive Effects on the Formation of Bulk Heterojunction Films. *Adv. Energ. Mater.* **5**, 1400975 (2015).
40 Credgington, D. & Durrant, J. R. Insights from Transient Optoelectronic Analyses on the Open-Circuit Voltage of Organic Solar Cells. *J. Phys. Chem. Lett.* **3**, 1465-1478 (2012).
41 Baran, D. *et al.* Qualitative Analysis of Bulk-Heterojunction Solar Cells without Device Fabrication: An Elegant and Contactless Method. *J. Am. Chem. Soc.* **136**, 10949-10955 (2014).
42 Vandewal, K., Tvingstedt, K., Gadisa, A., Inganas, O. & Manca, J. V. On the origin of the open-circuit voltage of polymer-fullerene solar cells. *Nat. Mater.* **8**, 904-909 (2009).
43 Deotare, P. B. *et al.* Nanoscale transport of charge-transfer states in organic donor-acceptor blends. *Nat. Mater.* **14**, 1130-1134 (2015).
44 Shuttle, C. G., Hamilton, R., Nelson, J., O'Regan, B. C. & Durrant, J. R. Measurement of Charge-Density Dependence of Carrier Mobility in an Organic Semiconductor Blend. *Adv. Funct. Mater.* **20**, 698-702 (2010).
45 Dang, B., He, J., Hu, J. & Zhou, Y. Large improvement in trap level and space charge distribution of polypropylene by enhancing the crystalline−amorphous interface effect in blends. *Polymer Int.* **65**, 371-379 (2016).
46 Baran, D. *et al.* Role of Polymer Fractionation in Energetic Losses and Charge Carrier Lifetimes of Polymer: Fullerene Solar Cells. *J. Phys.l Chem. C* **119**, 19668-19673 (2015).
47 Tremolet de Villers, B. J. *et al.* Removal of Residual Diiodooctane Improves Photostability of High-Performance Organic Solar Cell Polymers. *Chem. Mater.* **28**, 876-884 (2016).

48 García-Valverde, R., Cherni, J. A. & Urbina, A. Life cycle analysis of organic photovoltaic technologies. *Prog.Photov.* **18**, 535-558 (2010).
49 Espinosa, N., Hosel, M., Angmo, D. & Krebs, F. C. Solar cells with one-day energy payback for the factories of the future. *Energ. Environ. Sci.* **5**, 5117-5132 (2012).
50 Adams, J. *et al.* Air-processed organic tandem solar cells on glass: toward competitive operating lifetimes. *Energ. Environ. Sci.***8**, 169-176 (2015).

Figures

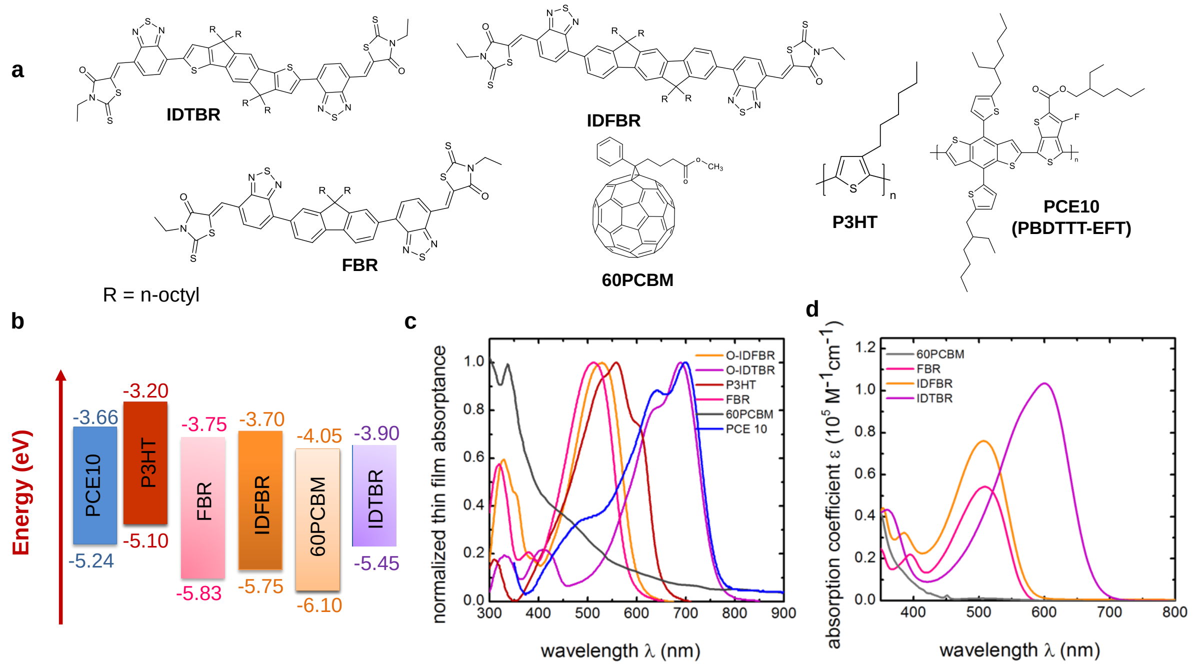

Figure 1 | Chemical structures, energy levels and optical properties of materials used in this study.

a Chemical structures of the acceptor molecules and the donor polymers used in this study. **b** Energy level diagram measured from thin films using cyclic voltammetry. **c** normalized thin film absorptions of neat donor and acceptor materials used in this study, and **d** absorption coefficients of 60PCBM, FBR, IDFBR and IDTBR solutions in chloroform solution (1× 10^{-5} M).

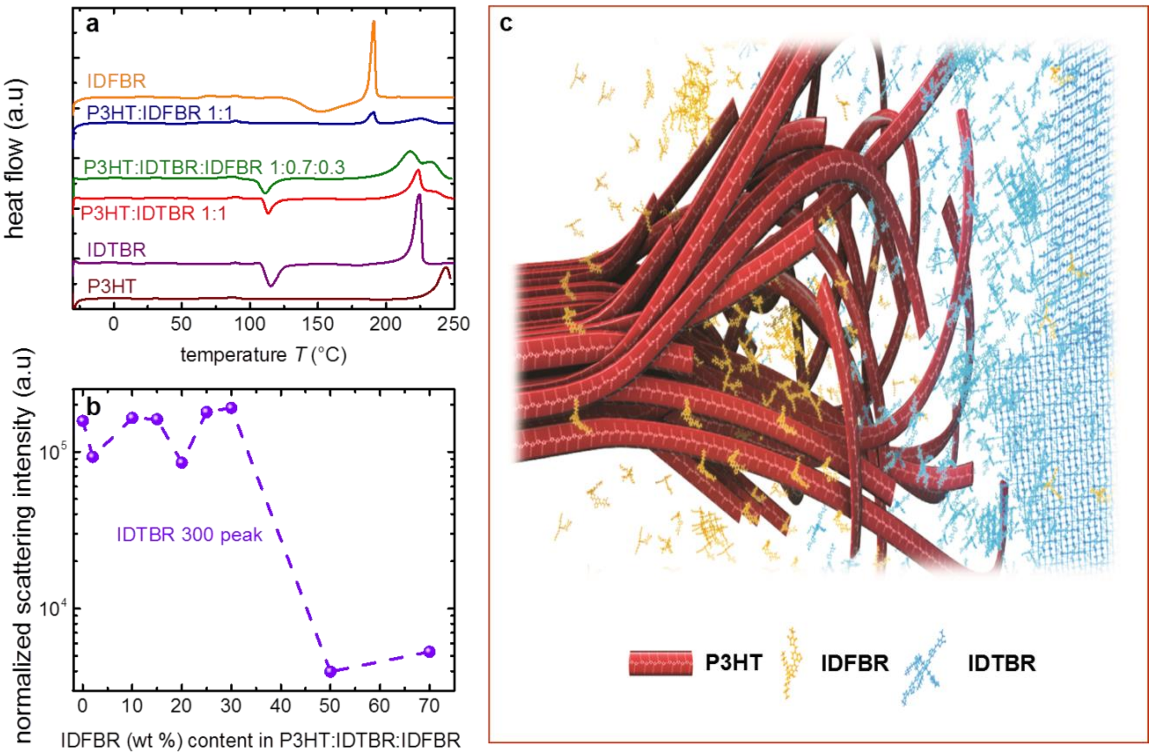

Figure 2 | Microstructural analysis of P3HT:IDTBR:IDFBR ternary blend. **a** The first DSC heating profiles of individual P3HT, IDTBR and IDFBR along with binary P3HT:IDTBR, P3HT:IDFBR and ternary P3HT:IDTBR:IDFBR blends. **b** 2D-GIWAXS profile for the P3HT:IDTBR:IDFBR blend with varying IDFBR loading, focusing on the characteristic crystallinity peak of IDTBR (300). **c** Visual illustration of the binary P3HT:IDTBR blend with IDFBR presence, wherein the crystallinity of both P3HT and IDTBR is preserved.

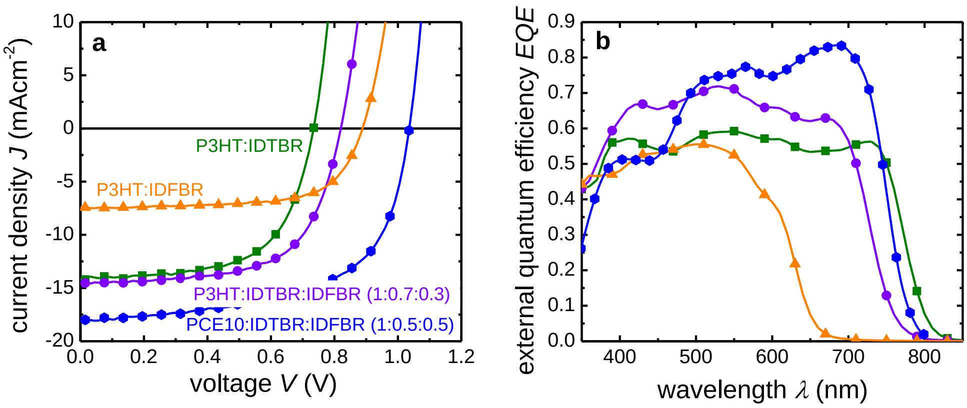

Figure 3 | Photovoltaic performances and EQE profiles of binary and ternary devices. **a** Current density-voltage (*J*-*V*) characteristics of binary and ternary devices under 1 sun illumination. The labels specify the donor:acceptor blends and ratios with P3HT and PCE10. **b** EQE spectra of corresponding photovoltaic devices.

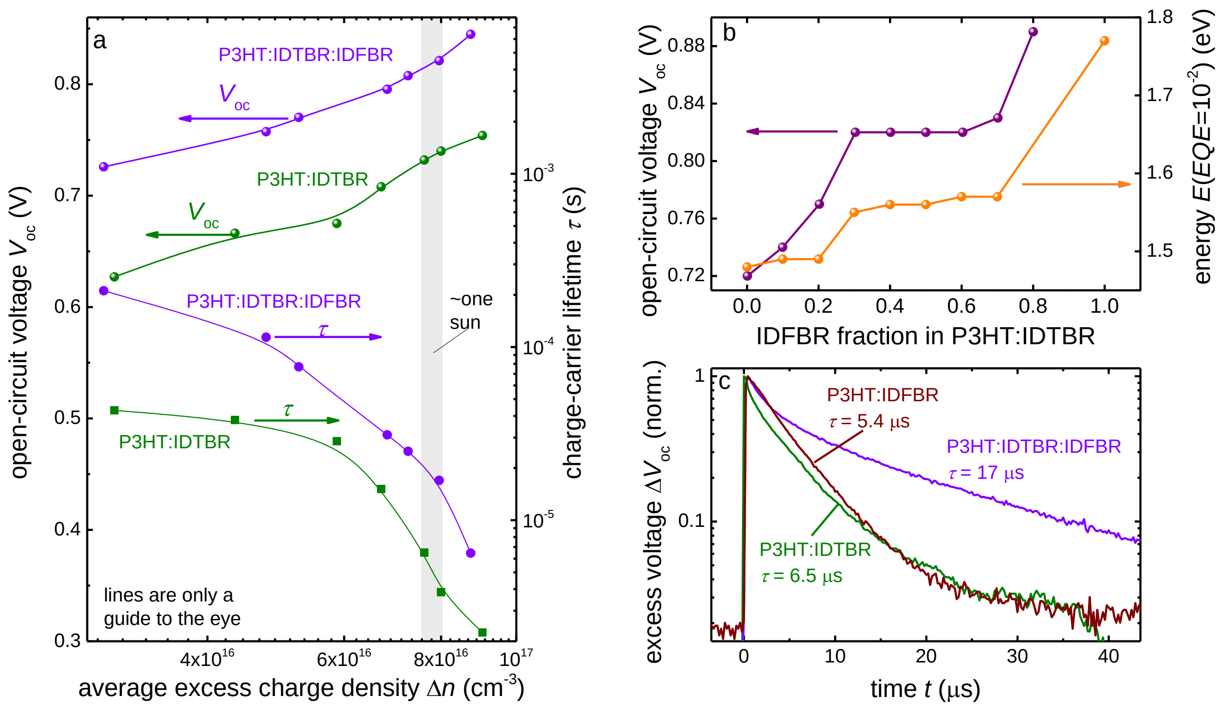

Figure 4 | Charge carrier dynamics of inverted P3HT:IDTBR and P3HT:IDTBR:IDFBR devices. **a** V_{oc} and recombination lifetime versus average excess charge density, **b** correlation between photon energies (at EQE = 10^{-2}) and V_{oc} of P3HT:IDTBR:IDFBR devices as a function of IDFBR content, **c** TPV data for corresponding P3HT:IDTBR and P3HT:IDTBR:IDFBR blends at V_{oc} in response to a small additional light pulse.

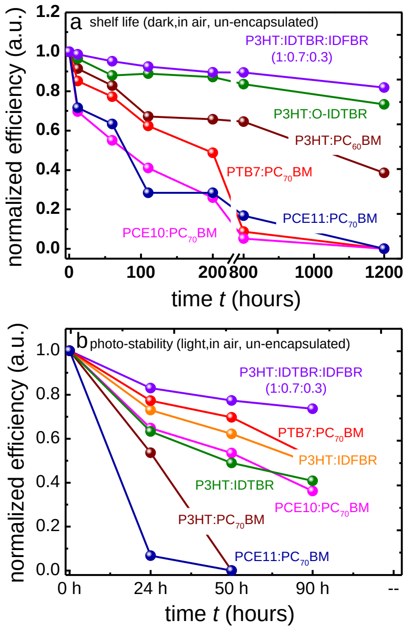

Figure 5 | Storage lifetime and photo-stability of P3HT:IDTBR:IDFBR and low bandgap high efficiency polymer:fullerene devices. **a** Shelf storage lifetime (dark, in air) comparison of P3HT:IDTBR:IDFBR device efficiencies with other polymer:fullerene systems. Devices were exposed to ambient conditions over a 1200 hours duration or until high devices did not show any diode behavior. **b** Photo-stability of P3HT:IDTBR:IDFBR device and polymer:fullerene solar cells (in air, un-encapsulated, under AM1.5 illumination at 1 sun) for 90h.

Table 1 | Photovoltaic parameters for binary and ternary blends.

Blend	Blend Ratio	J_{sc} (mA cm^{-2})	V_{oc} (V)	*FF*	**PCE** (%)
P3HT:IDTBR	1:1	13.9±0.2	0.72±0.01	0.60±0.03	6.3±0.1
P3HT:IDTBR:IDFBR	1:0.7:0.3	14.4±0.3	0.82±0.01	0.64±0.01	7.7±0.1
P3HT:IDTBR:FBR	1:0.7:0.3	12.2±0.2	0.80±0.01	0.62±0.01	6.0±0.1
P3HT:IDTBR:60PCBM	1:0.7:0.3	11.9±0.3	0.59±0.01	0.51±0.02	3.6±0.2
PCE10:IDTBR:IDFBR	1:0.5:0.5	17.2±0.1	1.03±0.01	0.6±0.01	11.0±0.4